



# Insight into hydroxyl groups in anchoring Ir single-atoms on vacancy-deficient rutile TiO<sub>2</sub> supports for selective catalytic oxidation of ammonia

Wenqing Xu <sup>a,b,1,\*</sup>, Yixi Wang <sup>a,1</sup>, Hong He <sup>b,c,d</sup>, Jun Yang <sup>a,d</sup>, Yang Yang <sup>a</sup>, Jinzhu Ma <sup>b,c,d</sup>, Chaoqun Li <sup>a</sup>, Tingyu Zhu <sup>a,b,\*</sup>

<sup>a</sup> CAS Key Laboratory of Green Process and Engineering, Institute of Process Engineering, Innovation Academy for Green Manufacture, Chinese Academy of Sciences, Beijing 100190, China

<sup>b</sup> Center for Excellence in Regional Atmospheric Environment, Institute of Urban Environment, Chinese Academy of Sciences, Xiamen 361021, China

<sup>c</sup> State Key Joint Laboratory of Environment Simulation and Pollution Control, Research Center for Eco-Environmental Sciences, Chinese Academy of Sciences, Beijing 100085, China

<sup>d</sup> University of Chinese Academy of Sciences, Beijing 100049, China



## ARTICLE INFO

### Keywords:

NO<sub>x</sub>  
NH<sub>3</sub>-SCO  
Ir/TiO<sub>2</sub> catalyst  
Hydroxyl groups  
I-SCR mechanism

## ABSTRACT

High-performance catalysts are extremely required for controlling NH<sub>3</sub> emission via selective catalytic oxidation (SCO), and the anchoring structural feature of active sites is a key prerequisite for developing them. This study confirms the importance of hydroxyl groups on vacancy-deficient reducible oxides as active groups. On the one hand, spontaneous atomic dispersion of active metal Ir is promoted by the abundant terminal hydroxyl groups. On the other hand, Ir cations anchor on the TiO<sub>2</sub> surface through exchange with H<sup>+</sup> in Ti-OH groups, and thus occupy the Brønsted acid sites. The adsorption strength of NH<sub>3</sub> is another key factor affecting the reaction rate-determining step, namely NH<sub>3</sub> dehydrogenation, which occurs at a faster rate in the coordinated L-NH<sub>3</sub> rather than the ionic B-NH<sub>4</sub><sup>+</sup>. Meanwhile, the coordinated L-NH<sub>3</sub> significantly avoids the competitive adsorption of water vapor in the NH<sub>3</sub>-SCO reaction by reducing the number of hydrogen bonding. The TOF of preferred 0.8Ir/TiO<sub>2</sub> sample is significantly higher than 0.2Ir/TiO<sub>2</sub> sample, although Ir is almost always atomic dispersed. Finally, NH<sub>3</sub> conversion is 85% in a wet circumstance (5% H<sub>2</sub>O) at 240 °C (GHSV = 85 000 h<sup>-1</sup>), with a N<sub>2</sub> selectivity of up to 65% on 0.8Ir/TiO<sub>2</sub> sample.

## 1. Introduction

NH<sub>3</sub> selective catalytic reduction (NH<sub>3</sub>-SCR) has become the most widely used technology to reduce the emission of nitrogen oxides (NO<sub>x</sub>) from both coal-fired industries and diesel engines [1–3]. The increasingly stringent emission regulations require that the injection amount of reducing agent usually exceeds the theoretical chemistry stoichiometric ratio, resulting in a serious problem of NH<sub>3</sub> slip [4]. Gaseous NH<sub>3</sub> is considered to be an important precursor of particulate matter with average diameters smaller than 2.5 μm (PM<sub>2.5</sub>), which contributes to the formation of haze and serious health issues [5,6]. In order to avoid potential harm to human health and the ecological environment, the allowable NH<sub>3</sub> slip concentration for the SCR system in industrial

industries such as coal-fired in China has been tentatively regulated to be less than 3 ppm [7].

Selective catalytic oxidation of NH<sub>3</sub> (hereafter referred to as NH<sub>3</sub>-SCO) into N<sub>2</sub> using catalysts has been regarded as a particularly promising process of decreasing the NH<sub>3</sub> emissions [8]. Noble metal catalysts, especially Pt- and Ag-based nanomaterials, have been widely investigated due to their excellent NH<sub>3</sub> conversion activity at the temperatures below 300 °C [9]. However, the active site is usually metallic aggregate particles, which lead to extremely low utilization of noble metals [10–13]. Iridium (Ir) is another typical noble metal, as reported in our previous research, the atomically dispersed Ir/TiO<sub>2</sub> catalyst has a clear activity advantage in NH<sub>3</sub>-SCO reaction based on the “electronic metal-support interaction” (EMSI) [14]. The construction of sufficient

\* Corresponding authors at: CAS Key Laboratory of Green Process and Engineering, Institute of Process Engineering, Innovation Academy for Green Manufacture, Chinese Academy of Sciences, Beijing 100190, China.

E-mail addresses: [wqxu@ipe.ac.cn](mailto:wqxu@ipe.ac.cn) (W. Xu), [tyzhu@ipe.ac.cn](mailto:tyzhu@ipe.ac.cn) (T. Zhu).

<sup>1</sup> Wenqing Xu and Yixi Wang contributed equally to this work.

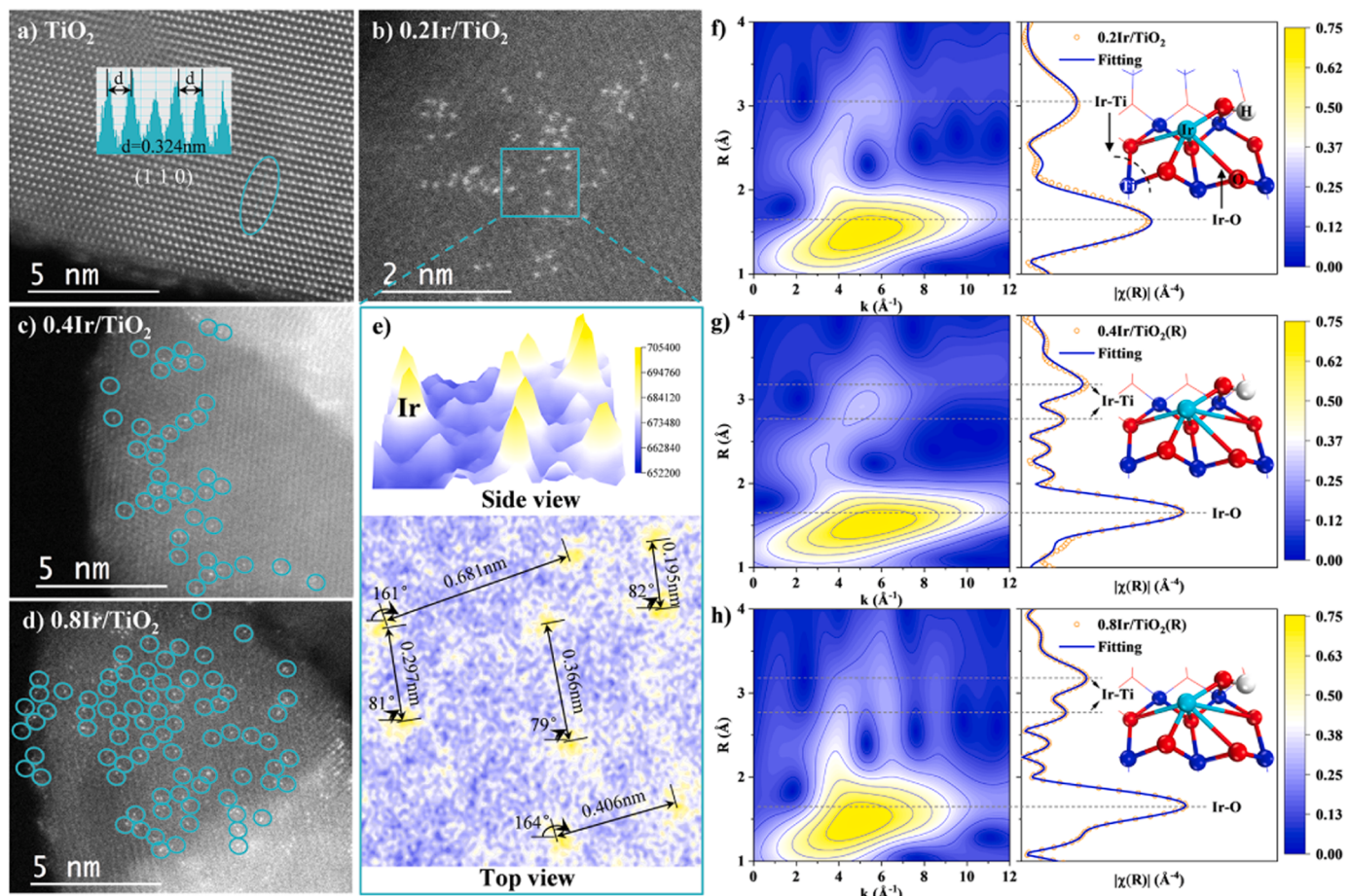


**Fig. 1.** HAADF-STEM images (a–e), WT-EXAFS contour plots and  $k^3$ -weighted EXAFS spectra (f–h) of Ir/TiO<sub>2</sub> samples with different Ir loadings (0.2, 0.4 and 0.8 wt. %). (a) TiO<sub>2</sub>, (b, e, f) 0.2Ir/TiO<sub>2</sub>, (c, g) 0.4Ir/TiO<sub>2</sub>, (d, h) 0.8Ir/TiO<sub>2</sub>.

active sites by single-atom anchoring provides an effective pathway to improve the utilization of loaded metal [15], which has attracted extensive attention and discussion in recent years [16]. It is generally believed that stable metal single-atom need to be obtained by modifying and regulating the anchoring sites on appropriate supports, which are played by active groups [17].

Previous experiments and DFT calculations suggest that the defects are the direct mediators for the interaction between reducible oxides (TiO<sub>2</sub> and CeO<sub>2</sub>, etc.) and active components [18–21]. Therefore, recent studies have focused on increasing the number of oxygen vacancies (labeled as O<sub>v</sub>) in order to promote high dispersion of loaded metals and strengthen the reaction rate-determining step, i.e., NH<sub>3</sub> dehydrogenation. However, compared to anatase TiO<sub>2</sub> with abundant O<sub>v</sub> [22], the capture of single-atom metals by O<sub>v</sub>-deficient rutile TiO<sub>2</sub> is also very common [23,24]. Some other active groups on reducible oxides must be responsible for this metal atom capture. Typically, Kwak et al. reported the critical role of unsaturated penta-coordinated Al<sup>3+</sup> (Al<sup>3+</sup><sub>penta</sub>) centers obtained by dehydration and dehydroxylation on Al<sub>2</sub>O<sub>3</sub> in trapping Pt metal [25]. Dutov and Wang et al. respectively proposed that the hydroxyl (–OH) groups on SiO<sub>2</sub> and Al<sub>2</sub>O<sub>3</sub> can maintain the stable dispersion of Ag [26,27]. However, the special role of these two sites in reducible oxide supports has not yet been elucidated. It is timely and necessary to reveal the anchoring mechanism of Ir species on TiO<sub>2</sub> for designing more effective Ir/TiO<sub>2</sub> catalysts or optimizing current catalysts using TiO<sub>2</sub> as the supports for NH<sub>3</sub>-SCR, NH<sub>3</sub>-SCO materials need to meet high requirements for low-temperature activity and the resistance of flue gas components (e.g., water vapor) [28,29]. Hence, the reaction mechanism

of these active groups in the rate-determining step, namely NH<sub>3</sub> dehydrogenation, has become another prerequisite for developing high-performance catalysts.

In this work, Ir/TiO<sub>2</sub> samples with different Ir loadings are synthesized for correlating the O<sub>v</sub>, unsaturated centers and –OH groups with Ir anchoring and calculating the binding energies of Ir at these sites. It is found that the relative amount of terminal –OH groups dominate the dispersion of Ir cations. While the type of acid sites on Ir/TiO<sub>2</sub> surface affects the NH<sub>3</sub> dehydrogenation rate and the competitive adsorption by water vapor. The conclusion improves the theoretical system of single-atom catalyst supported by reducible oxides and reveals the importance of hydroxyl groups as metal–support interactions media in catalytic reactions, which is significant for designing high-utilization catalysts.

## 2. Experimental

### 2.1. Catalyst preparation

Rutile TiO<sub>2</sub> was purchased from Aladdin chemicals. In detail, 6 g of TiO<sub>2</sub> was added in 250 mL of deionized water and the corresponding volume of iridium acetate solution (10 g·L<sup>−1</sup>) was added. Typically, excess water was removed by a rotary evaporator at 60 °C under vacuum after stirring in water solvent for 1 h at about 25 °C. Then, the samples were dried 12 h at 110 °C and calcined at 400 °C in 20% O<sub>2</sub> + N<sub>2</sub> for 4 h (denoted as 0.2Ir/TiO<sub>2</sub>, 0.4Ir/TiO<sub>2</sub>, 0.8Ir/TiO<sub>2</sub> with Ir mass loading of 0.2, 0.4 and 0.8 wt.%, respectively). Finally, the samples were crushed and passed through a 40–60 mesh sieve before testing.

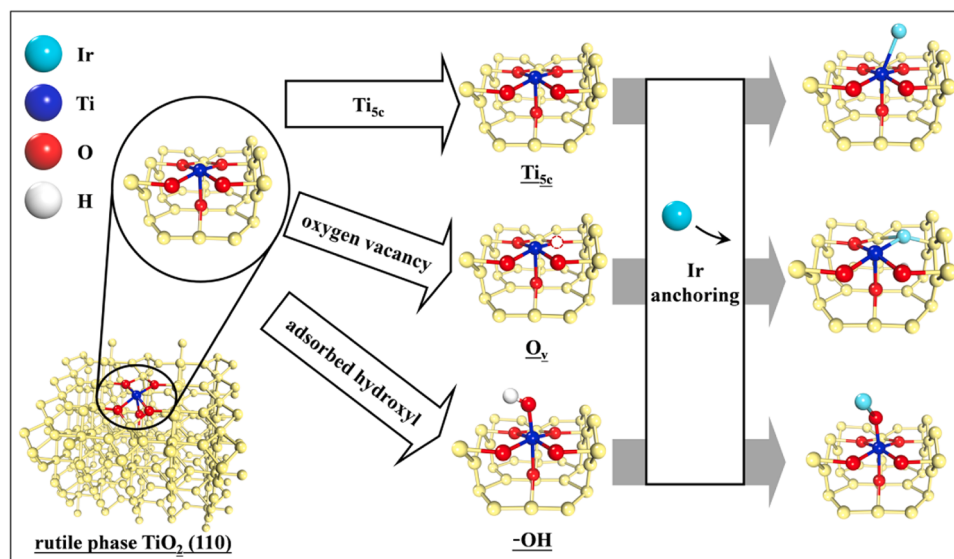


**Fig. 2.** A diagram showing three possible processes of Ir anchoring (Some of the periodic atoms in the model are replaced in yellow for emphasis).

## 2.2. Catalyst characterization

The samples were characterized by using various methods, including  $N_2$  adsorption/desorption, High-angle annular dark-field scanning transmission electron microscopy (HAADF-STEM), X-ray Absorption Fine Structure (XAFS), X-ray photoelectron spectroscopy (XPS), Electron paramagnetic resonance (EPR),  $H_2$ -temperature-programmed reduction ( $H_2$ -TPR),  $NH_3$ -temperature-programmed desorption ( $NH_3$ -TPD), in situ diffuse reflexions infrared fourier transformations spectroscopy (DRIFTS), and density functional theory (DFT) method. Bulk composition and the metal dispersion was measured by ICP-OES and  $H_2$  chemisorption conducted on an Auto Chem II 2920. Detailed procedures are provided in [Supporting Information](#).

## 2.3. Catalytic evaluations

The activity measurements of  $NH_3$ -SCO under atmospheric pressure were completed using a quartz tubular continuous flow reactor (inner diameter = 6 mm), with each sample weighing approximately 200 mg. The feed gas contained 400 ppm  $NH_3$ , 10%  $O_2$ , 5%  $H_2O$  (when used) and balanced  $N_2$ . The total flow rate is 300  $mL \cdot min^{-1}$  with a gas hourly space velocity (GHSV) of 85 000  $h^{-1}$ . The gas concentrations of  $NH_3$ ,  $N_2O$ ,  $NO$ , and  $NO_2$ , were real time analyzed using an online FTIR spectrometer equipped with a DTGS detector. Turnover frequencies (TOFs) were obtained in a separate experiment where the conversion of  $NH_3$  was kept below 30% by varying the GHSV (85 000–340 000  $h^{-1}$ ) with negligible heat and mass-transfer effects, and which are calculated using the Ir basis. The  $NH_3$  conversion ( $X_{NH_3}$ ),  $N_2$  selectivity ( $S_{N_2}$ ) and TOF were calculated as below:

$$X_{NH_3} = \left[ 1 - \frac{NH_3(\text{out})}{NH_3(\text{in})} \right] \times 100\% \quad (1)$$

$$S_{N_2} = \frac{[NH_3(\text{in}) - NH_3(\text{out})] - 2 \times N_2O(\text{out}) - NO(\text{out}) - NO_2(\text{out})}{[NH_3(\text{in}) - NH_3(\text{out})]} \times 100\% \quad (2)$$

$$TOF = \frac{X_{NH_3} \times Q \times NH_3(\text{in}) / (60 \times V_m)}{m \times w \times D/M} \quad (3)$$

Where  $Q$ ,  $V_m$ ,  $m$ ,  $w$ ,  $D$ ,  $M$  are total flow rate, molar volume of gas, catalyst quality, loading of Ir, dispersion of Ir, molar mass of Ir atom, respectively.

The catalysts were stabilized for 120 min at each temperature point, and the gas concentrations were recorded for the last 10 min and averaged.

## 3. Results and discussion

### 3.1. Dispersion and coordination state of Ir species

Aberration-corrected HAADF-STEM measurements were performed to investigate the Ir dispersion for Ir/TiO<sub>2</sub> catalysts with different loading. As shown in [Fig. 1a](#), the lattice spacing of TiO<sub>2</sub> is 0.324 nm, corresponding to the (110) plane of its rutile phase (PDF No. 00-021-1276) [30,31]. According to the principle of Z-contrast imaging, the image intensity of an element is proportional to the square of its atomic number (Z) [32]. Therefore, the image intensity of Ir (Z = 77) atoms is higher than that of Ti (Z = 22) atoms. The isolated bright spots belonging to single-atom Ir<sub>1</sub> species can be clearly identified for all the Ir/TiO<sub>2</sub> samples [33], as marked by the blue circles ([Fig. 1b-d](#)). It should be noted that the distribution of single-atom Ir<sub>1</sub> is random on the surface of TiO<sub>2</sub> substrate for loaded Ir/TiO<sub>2</sub> samples, rather than embedded in the lattice. The randomness can be further analyzed in the selected-area intensity surface plot, and the distance and angle between two atoms vary greatly within the selected range ([Fig. 1e](#)). The failure to form ordered crystal structures is an important feature of atomic dispersion.

XAFS was carried out to further understand the local atomic environment and electronic structure of the Ir/TiO<sub>2</sub> samples [34]. The discrepancy in oscillation between Fourier transform (FT) EXAFS spectra ([Fig. S1](#)) indicates the difference in the coordination structure of Ir species. As shown in [Fig. 1f-h](#), combining the peaks displayed in R-space with the specific signals of elements in k and R-space provided from wavelet transform (WT) analysis can provide a more intuitive interpretation [35,36]. The maximum intensity of all the Ir/TiO<sub>2</sub> samples appeared around 5.3 Å<sup>-1</sup>, corresponding to the Ir-O contribution. Based on the EXAFS fitting curves ([Table S1](#)), other amplitudes at the second shell were attributed to Ir-Ti contribution, with a significant difference between its bond length (ranging from 3.134 to 3.489 Å) and Ir-O-Ir bond length (3.229 and 3.594 Å). It was observed that there is no contribution of Ir-Ir or Ir-O-Ir, confirming that isolated single atomic sites are dominant for Ir loading of 0.2–0.8 wt.% in Ir/TiO<sub>2</sub> samples [33,37]. As summarized in [Table S1](#), the average coordination number (CN) of Ir-O is between 5–6, and that of Ir-Ti is between 4–6. The total CN of Ir cation is 9, 10.8, 11.3 in turn, with the increase of Ir loading. The difference in CN of Ir-O in the three samples may be due to the

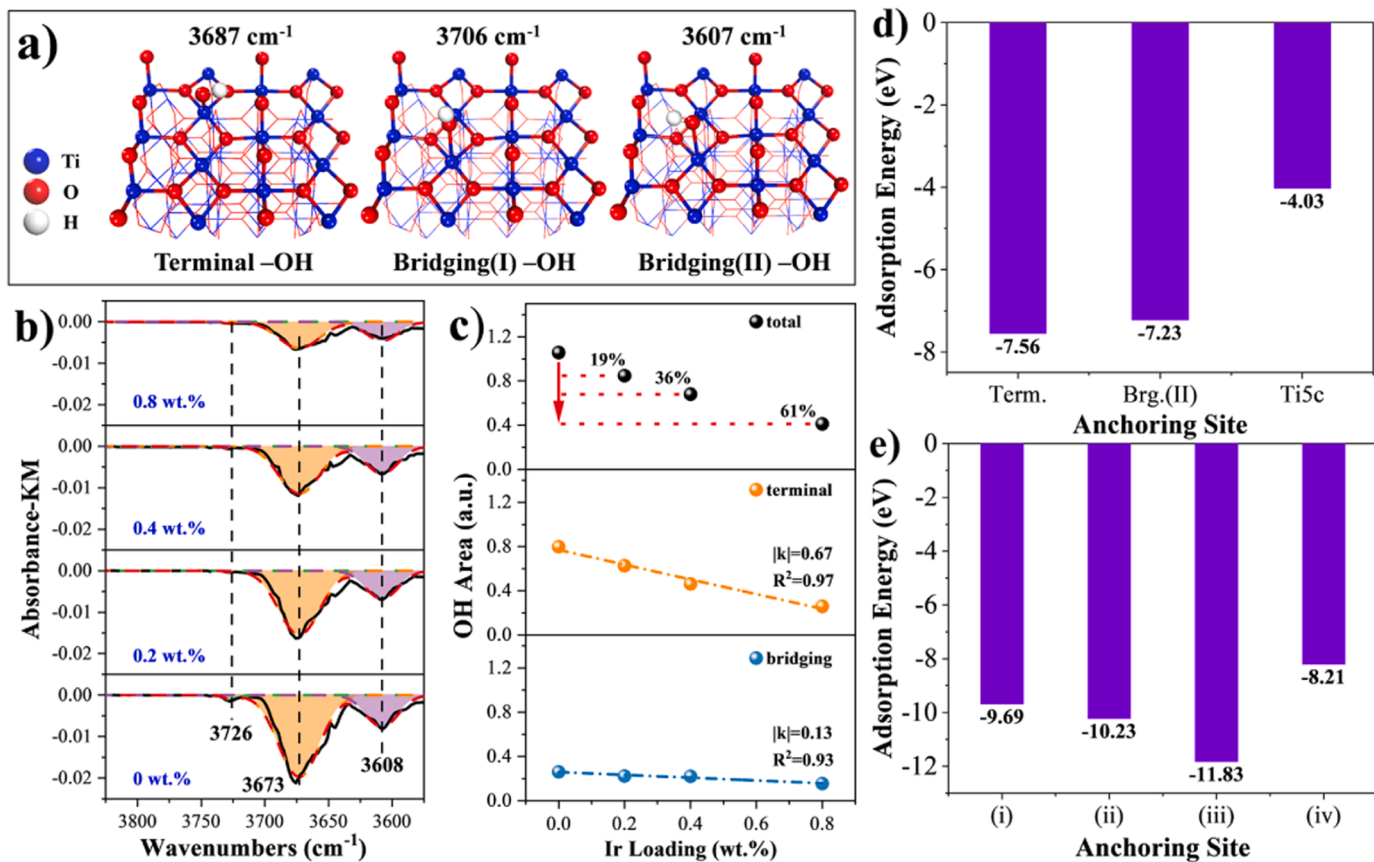


**Fig. 3.** DFT and in situ DRIFTS of Ir/TiO<sub>2</sub> samples. (a) Optimized periodic models of the hydroxylated TiO<sub>2</sub> (110) surface, (b) Peak resolution of -OH consumption peaks after in situ DRIFTS of NH<sub>3</sub> adsorption over Ir/TiO<sub>2</sub> with different Ir loadings (0, 0.2, 0.4 and 0.8 wt.%) at 40 °C, (c) Relationship between Ir loading and peak areas of -OH groups over Ir/TiO<sub>2</sub>, (d) Ir adsorption energy over single site on terminal -OH (labeled term.), bridging(II) -OH (labeled brg.) and Ti<sub>5c</sub>, (e) Ir adsorption energy in multiple OH complex environment, and the structures of anchoring site are as follows: (i) term.+term.+Ti<sub>5c</sub> (Fig. S10), (ii) term.+term.+term. (Fig. S11), (iii) term.+term.+brg. (Fig. S12), (iv) brg.+term.+Ti<sub>5c</sub> (Fig. S13).

adsorption of H<sub>2</sub>O in the air by Ir cations to form new hydroxyl groups. It is confirmed that the structure of Ir and Ti atoms bridged by O atoms is shown in the inset.

### 3.2. Analysis of the anchoring sites

Three possible anchoring sites, i.e., unsaturated penta-coordinated Ti cation (Ti<sub>5c</sub>), O<sub>v</sub>, and -OH groups, have been reported on oxide surfaces (both reducible and nonreducible oxides have been referenced). Fig. 2 shows the relaxed structure of the dominant (110) surface on TiO<sub>2</sub> [38]. First of all, abundant Ti<sub>5c</sub> sites expose on the surface. It has been widely reported that the Ti<sub>5c</sub> cations provide repulsive lateral force or bridging sites for the adsorption and migration of molecules or atoms, such as CO<sub>2</sub>, CO [39,40], and Au atom [41]. Kwak et al. proposed that the coordinative saturation of unsaturated sites is the driving force for metal atom anchoring on nonreducible oxides [25]. Therefore, as unsaturated coordinating cations, Ti<sub>5c</sub> should be marked as the first type of anchoring site. In addition, the previous description mentioned that the defect sites are the direct mediators for electron transfer between the reducible oxide support and the loaded components. The atomic defects formed on the surface of TiO<sub>2</sub> introduce excess electrons into the surrounding lattice, leading to suitable adsorption sites such as O<sub>v</sub> [42,43]. The distribution and dynamics of O<sub>v</sub> can significantly affect the dispersion and shape of metal particles. For example, Au particles do not bind to a perfect TiO<sub>2</sub> surface, but have a binding energy of about 1.6 eV at per defect [21]. The surface O<sub>v</sub> on defective TiO<sub>2</sub> nanosheets could effectively stabilize the single-atom Pt<sub>1</sub> by building a Ti-Pt-Ti structure [44]. Therefore, O<sub>v</sub> is marked as the second type of anchoring site. The

last possible anchoring environment is related to the -OH groups, which is affected by the preparation environment. Wang et al. revealed that Al<sup>3+</sup><sub>penta</sub> sites could be easily coordinatively saturated through the interaction with H<sub>2</sub>O, and the single-atom Ag<sub>1</sub> is anchored by the terminal Al-OH group through oxygen bridges [27]. There are enough water molecules in the air to hydroxyl on the oxide surface, providing a third site for Ir anchoring.

The existence of O<sub>v</sub> over samples was further verified by electron paramagnetic resonance (EPR) experiments. TiO<sub>2</sub> sample exhibits a pair of steep peaks with a symmetric distribution (Fig. S2) in accordance with a signal at  $g = 2.008$ , an indication of electron trapping at O<sub>v</sub> [45]. In contrast, no O<sub>v</sub> signal is observed on all the Ir/TiO<sub>2</sub> samples, unambiguously proving that the contribution of O<sub>v</sub> to Ir anchoring is limited. The O 1 s XPS spectra were used to quantitatively compare the amount of O<sub>v</sub>. The peaks at 531.38 eV, 530.88 eV and 529.77 eV belong to surface-adsorbed oxygen species (labeled O<sub>surf</sub>), surface O<sub>v</sub> for TiO<sub>2</sub>, and lattice oxygen in TiO<sub>2</sub> (labeled O<sub>latt</sub>), respectively [46–49]. The percentage of O<sub>v</sub> in surface O species for TiO<sub>2</sub> sample is calculated to be 2.90% (Table S2), since rutile phase is thermodynamically stable with weak electron-hole separation ability [46,50]. While the percentage of O<sub>surf</sub> decreased from 14.97% to 8.51% as the Ir loading increases. O<sub>surf</sub> species include adsorbed molecular water, and -OH, etc., where -OH groups are usually dominant [51,52].

Two types of OH groups could be identified in TiO<sub>2</sub>, i.e., terminal -OH group and bridging -OH group, as shown in Fig. S3. According to previous reports, each oxygen atom is surrounded by two Ti atoms and one H atom at the center of a triangle. Since the sides of the triangle have different lengths, there may be two types of the bridging -OH group

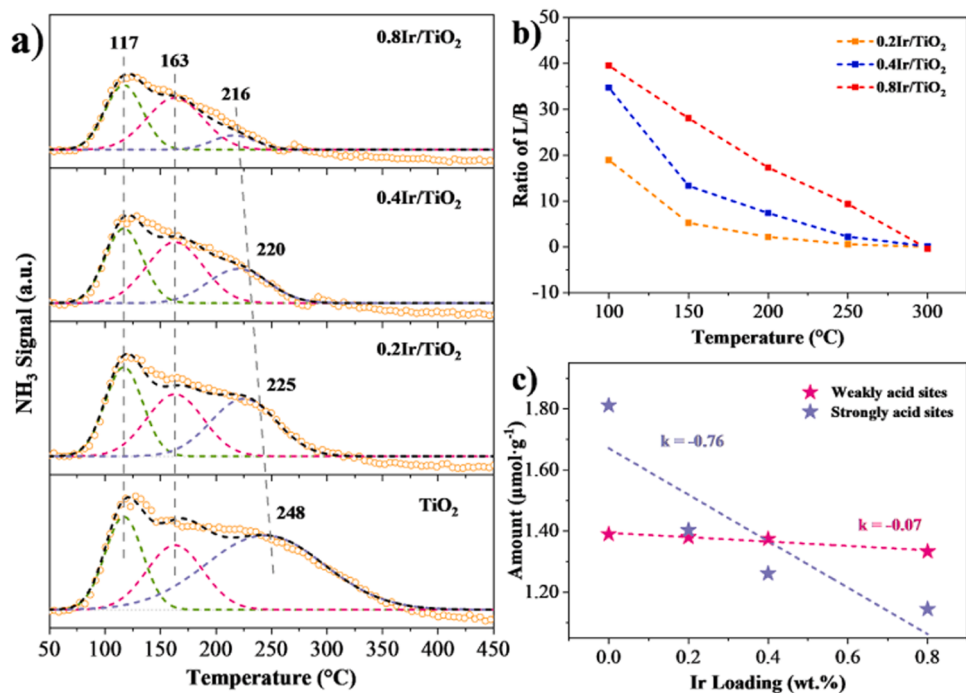


**Fig. 4.** The chemical properties of Ir/TiO<sub>2</sub> samples with different Ir loadings (0, 0.2, 0.4 and 0.8 wt.%). (a) TPD profiles of NH<sub>3</sub>, (b) Changes in the relative amount of Lewis acid sites and Brønsted acid sites (L/B) with temperature according to in situ DRIFTS, (c) Amount of acid sites according to NH<sub>3</sub>-TPD.

(labeled bridging(I) -OH and bridging(II) -OH, respectively) [53]. Optimized periodic models of the hydroxylated TiO<sub>2</sub> (110) surface were shown in Fig. 3a. Three O-H stretching frequencies corresponding to two types of -OH groups were calculated [54], wherein, 3687 cm<sup>-1</sup> can be assigned to terminal -OH, while 3706 cm<sup>-1</sup> and 3607 cm<sup>-1</sup> can be assigned to bridging -OH. The type and relative percentage of -OH groups can be detected by in situ DRIFTS analysis using NH<sub>3</sub> as a probe [55,56]. Once Ir atoms occupy some of the -OH groups on TiO<sub>2</sub>, the intensities of negative OH peaks would decrease since fewer OH sites are available for NH<sub>3</sub> adsorption [27]. The calculation results of stretching frequency are used to guide the attribution of OH bands in the spectra (Fig. 3b). The negative bands at 3726 cm<sup>-1</sup>, 3673 cm<sup>-1</sup> and 3608 cm<sup>-1</sup> are assigned to the occupation of isolated -OH group of bridging(I) -OH, terminal -OH and bridging(II) -OH [53,57].

As shown in Fig. 3c, the total -OH area decreases by 19%, 36% and 61% with the increase of Ir loading (0.2, 0.4 and 0.8 wt.%), indicating that -OH sites are partially occupied by Ir species. Individual peak areas were calculated by integration and then the correlation between the Ir loading and the consumption of different types of -OH groups were analyzed. The area of terminal -OH group changes more significantly with the increase of Ir loading ( $|k| = 0.67$ ), which is higher than the slope of the bridging -OH group ( $|k| = 0.13$ ). The linear correlation between the area of terminal -OH group and Ir loading capacity is 0.97, which is slightly higher than that of bridging -OH group (0.93). These results strongly support the anchoring of Ir species on the TiO<sub>2</sub> surface through their interaction with -OH groups, particularly with terminal -OH group. Although the specific surface area of rutile TiO<sub>2</sub> is significantly lower than that of anatase TiO<sub>2</sub> (Table S3), a sufficient amount (75.4%) of terminal -OH groups actually provides more possibilities for Ir cations disperse at atomic level (Fig. S4).

The anchoring effects of the -OH groups were verified by DFT theoretical calculations, and the binding energy of Ir and Ti<sub>5c</sub> site was compared. An optimized periodic model of the rutile TiO<sub>2</sub> (110) surface were shown in Fig. S5. The periodic models of terminal -OH, bridging -OH and Ti<sub>5c</sub> site were constructed and optimized (Figs. S6–S9). In Fig. 3d, the binding energies of Ir anchored at the three single sites (terminal -OH, bridging(II) -OH and Ti<sub>5c</sub> site) are negative, indicating

that all three anchoring sites have strong affinity for Ir. Furthermore, the lowest binding energy occurred at terminal -OH site (-7.56 eV). At the same time, the original Ti-O bond between the -OH group and TiO<sub>2</sub> support is cut off due to the intervention of Ir species. It is confirmed that Ir atom cannot directly anchor at a certain -OH group, but forms a multi-coordination structure with surrounding atoms. In contrast, the Ir species cannot be stably adsorbed on the bridging(I) -OH site. The coordination environment of terminal -OH as the center is enriched by various -OH groups, as shown in Fig. 3e, and the binding energy of Ir anchored at the terminal -OH site is further reduced. The optimized model details are shown in Figs. S10–S13. Especially when the two sides of the terminal -OH anchoring center are filled with one terminal -OH and one bridging -OH respectively, the binding energy of Ir reduces to -11.83 eV. These results confirm that Ir cations preferentially displace H<sup>+</sup> in Ti-OH to disperse, and the coordination structure is also influenced by the surrounding environment. The most stable coordination structure should be grateful for the simultaneous consumption of multiple -OH groups, and the CN is close to the fitting result of XAFS.

### 3.3. Surface acidity and NH<sub>3</sub>-SCO reaction mechanism

It is well known that the -OH group, as one of Brønsted acid sites, plays an important role in the NH<sub>3</sub>-SCO reaction [13]. Therefore, we evaluated the acidities of the samples after loading Ir through NH<sub>3</sub>-TPD analyses. The amount of physisorbed NH<sub>3</sub> (located at 117 °C in Fig. 4a) was affected by a decrease of specific surface area (Table S3). While the loading of Ir inhibits the chemisorption of NH<sub>3</sub>, and the desorption peaks at 163 °C and 216–248 °C are attributed to the weakly acid sites and the strongly acid sites, respectively [58,59]. Actually, the strength of the strongly acid sites decreases with the increase of Ir loading. As shown in Fig. S14 and Fig. 4b, although mutual conversion would occur between ionic NH<sub>4</sub><sup>+</sup> adsorbed on the Brønsted acid sites (B-NH<sub>4</sub><sup>+</sup> at 1436 cm<sup>-1</sup>) and NH<sub>3</sub> coordinated to the Lewis acid sites (L-NH<sub>3</sub> at 1178 cm<sup>-1</sup>) in the low temperature range (150–250 °C), the B-NH<sub>4</sub><sup>+</sup> is more stable than the L-NH<sub>3</sub> since it has not fully desorbed at 300 °C. The relative content of Lewis acid sites decreases with increasing temperature for all Ir/TiO<sub>2</sub> samples. Therefore, the strongly acid sites are mainly served by the

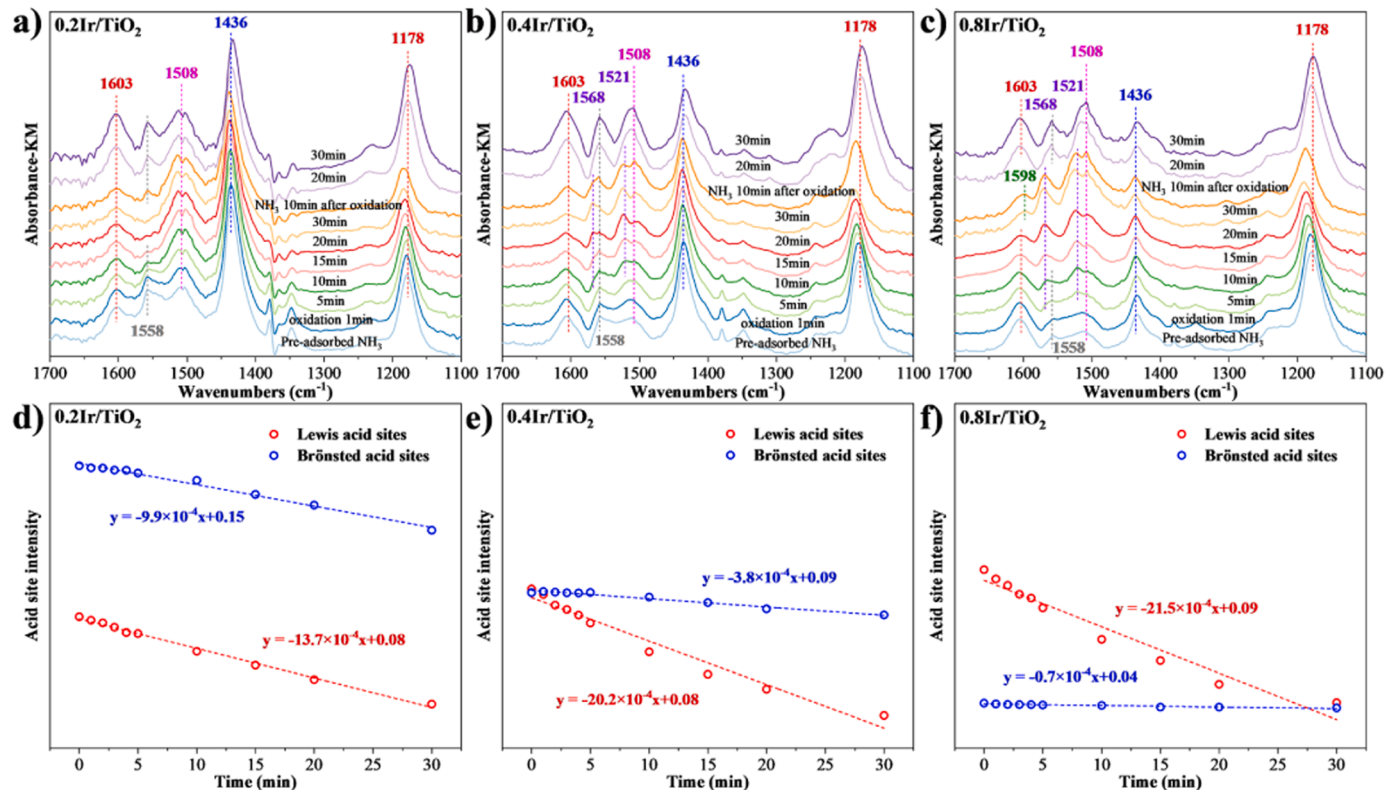


**Fig. 5.** In situ DRIFTS results for the reaction between O<sub>2</sub> and pre-adsorbed NH<sub>3</sub> species over (a) 0.2Ir/TiO<sub>2</sub>, (b) 0.4Ir/TiO<sub>2</sub>, (c) 0.8Ir/TiO<sub>2</sub>. And the consumption rate of Lewis and Brønsted acid sites under O<sub>2</sub> on (d) 0.2Ir/TiO<sub>2</sub>, (e) 0.4Ir/TiO<sub>2</sub>, (f) 0.8Ir/TiO<sub>2</sub>. Reaction conditions: 400 ppm NH<sub>3</sub>, 10% O<sub>2</sub> in N<sub>2</sub> at 200 °C.

Brønsted acid sites. We believe that the loading of Ir cation acts as electron donating groups, reducing the degree of charge delocalization on the neighboring oxygen atom compensated by the proton [60]. Moreover, the amount of acid sites could be quantified by deconvolution. In Fig. 4c, the slope is used to reflect the degree of decrease in the number of acid sites, which reaches  $-0.76$  in strongly acid sites and is only  $-0.07$  in weakly acid sites. The decrease in the amount of strongly acid sites is due to Ir cation occupying some of the  $-\text{OH}$  groups, but new Lewis acid sites are formed at the electron-deficient area as the intensity of EMSI between support and Ir cation gradually increased [61].

The reaction mechanism of NH<sub>3</sub>-SCO on Ir/TiO<sub>2</sub> catalysts was investigated at 200 °C by using in situ DRIFTS. Dynamic spectra of injecting O<sub>2</sub> onto pre-adsorbed NH<sub>3</sub> samples are presented in Fig. 5a-c. According to previous studies, the bands at 1603, 1178 cm<sup>-1</sup> were ascribed to NH<sub>3</sub> coordinated to the Lewis acid sites (L-NH<sub>3</sub>), the bands at 1436 cm<sup>-1</sup> was related to ionic NH<sub>4</sub><sup>+</sup> adsorbed on the Brønsted acid sites (B-NH<sub>4</sub><sup>+</sup>), the bands at 1558 cm<sup>-1</sup> and 1508 cm<sup>-1</sup> were due to  $-\text{NH}_2$  species and monodentate nitrate, respectively [62-65]. It confirms that the role of O<sub>latt</sub> in dehydrogenation and oxidation to form monodentate nitrate cannot be ignored. For 0.2Ir/TiO<sub>2</sub> sample, the peaks of L-NH<sub>3</sub>, B-NH<sub>4</sub><sup>+</sup> and  $-\text{NH}_2$  species slowly decreased with the injection of O<sub>2</sub>, while the peak of monodentate nitrate become more pronounced. When the injection of O<sub>2</sub> was cut off and the sample was exposed to NH<sub>3</sub> again, the peak of these adsorbed species almost returned to the initial level. This indicates that nitrate species are key intermediates after the dehydrogenation of adsorbed NH<sub>3</sub> and can be reduced by subsequent gas-phase NH<sub>3</sub>, following the internal selective catalytic reduction (i-SCR) mechanism, and is usually responsible for high N<sub>2</sub> selectivity [8, 66-68]. The bidentate and bridging nitrates were also observed at the same temperature on 0.4Ir/TiO<sub>2</sub> and 0.8Ir/TiO<sub>2</sub> samples. Among them, the peaks of bidentate nitrate (1568 and 1521 cm<sup>-1</sup>) appeared 10 min after O<sub>2</sub> injection on 0.4Ir/TiO<sub>2</sub> but appeared 5 min after O<sub>2</sub> injection on 0.8Ir/TiO<sub>2</sub>. While the peak of bridging nitrate (1598 cm<sup>-1</sup>) were

observed at 30 min only on 0.8Ir/TiO<sub>2</sub> [69,70].

The peak consumption rate of Lewis and Brønsted acid sites during the injection of O<sub>2</sub> were fitted in Fig. 5d-f. The initial acid site intensity was determined by the amount of acid sites on the Ir/TiO<sub>2</sub> samples, and L-NH<sub>3</sub> gradually dominated with the increase of Ir loading compared to B-NH<sub>4</sub><sup>+</sup>. And the consumption rate of L-NH<sub>3</sub> was always higher than that of B-NH<sub>4</sub><sup>+</sup>. On the 0.2Ir/TiO<sub>2</sub> sample, the consumption rate of L-NH<sub>3</sub> was about  $-13.7 \times 10^{-4}$ , only slightly higher than the consumption rate of B-NH<sub>4</sub><sup>+</sup> ( $-9.9 \times 10^{-4}$ ). However, the difference between them gradually increased as L-NH<sub>3</sub> dominated. On the 0.4Ir/TiO<sub>2</sub> sample, the consumption rate of L-NH<sub>3</sub> increased to  $-20.2 \times 10^{-4}$ , while the consumption rate of B-NH<sub>4</sub><sup>+</sup> decreased to  $-3.8 \times 10^{-4}$ . While the consumption rate of B-NH<sub>4</sub><sup>+</sup> was close to zero, and the active species were almost entirely L-NH<sub>3</sub> ones on 0.8Ir/TiO<sub>2</sub> sample. These results indicate that both L-NH<sub>3</sub> and B-NH<sub>4</sub><sup>+</sup> can convert to nitrates under the reaction of O<sub>2</sub>, and the dehydrogenation rate of L-NH<sub>3</sub> is higher than that of B-NH<sub>4</sub><sup>+</sup>, making it easier to support the generation of bidentate and bridging nitrates at low temperatures.

### 3.4. Electron effect and NH<sub>3</sub>-SCO performance

As previously reported [37,71-73], the energy position of the white line is highly sensitive to metals valence states, due to it is proportional to the d-orbital density of states. For Ir/TiO<sub>2</sub> samples, their white line intensity was significantly higher than that of Ir foil, suggesting that Ir species carry positive charges (Fig. S1). Interestingly, the higher integrated white line intensity appeared with increasing Ir load increases indicates the emptier d-orbital states (d holes) and higher oxidation states of 0.8Ir/TiO<sub>2</sub> than 0.4Ir/TiO<sub>2</sub> or 0.2Ir/TiO<sub>2</sub>, which may lead to enhanced EMSI [61,74,75]. This is supported by the fitting results of Ir-O bonding distance in Table S1, which are close to the IrO<sub>2</sub> standard sample. The electronic perturbations caused by EMSI can be described as the change of the d-band center relative to the Fermi level [75,76]. An

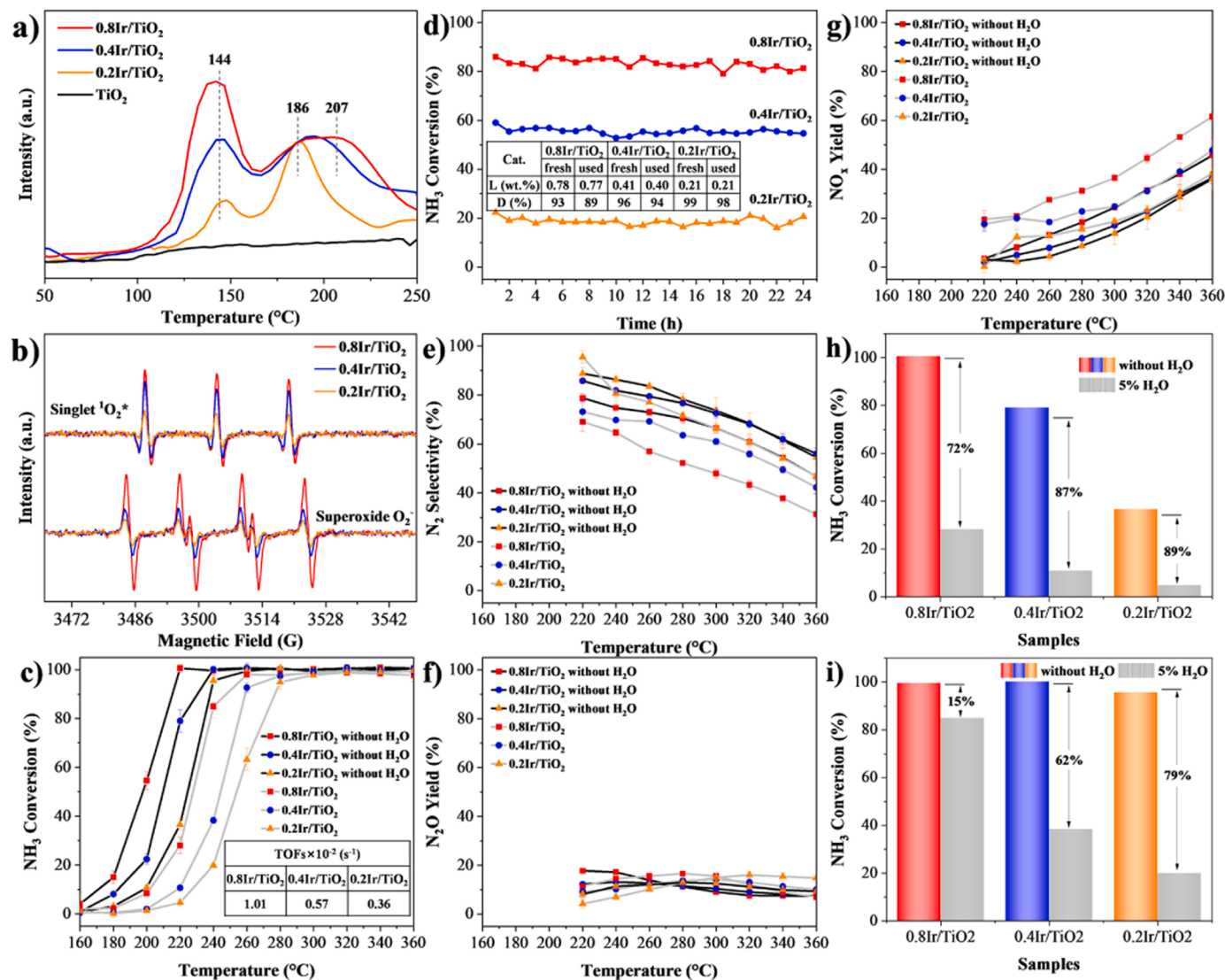


**Fig. 6.** Electron effect and NH<sub>3</sub>-SCO performance of Ir/TiO<sub>2</sub> catalysts with different Ir loadings (0.2, 0.4 and 0.8 wt.%). (a) TPR profiles of H<sub>2</sub>, (b) EPR signals of singlet <sup>1</sup>O<sub>2</sub><sup>\*</sup> (upper) with 2,2,6,6-tetramethyl-4-piperidone (TEMP) and superoxide O<sub>2</sub><sup>-</sup> (down) with 5,5-dimethyl-1-pyrroline N-oxide (DMPO) spin trapping agent, (c) NH<sub>3</sub> conversion, (d) 24 h stability tests at 210 °C, together with Ir loading (L) and Ir dispersion (D) for fresh and used samples. (e) N<sub>2</sub> selectivity, (f) N<sub>2</sub>O yield, (g) NO<sub>x</sub> yield. Reaction conditions: 400 ppm NH<sub>3</sub>, 10% O<sub>2</sub> and 5% H<sub>2</sub>O (when used) in N<sub>2</sub>, GHSV = 85 000 h<sup>-1</sup>. TOFs were obtained at 200 °C, and the reaction conditions were as below: 400 ppm NH<sub>3</sub> and 10% O<sub>2</sub> in N<sub>2</sub>, GHSV = 85 000–340 000 h<sup>-1</sup>, (h) Contrast of NH<sub>3</sub> conversion in dry and wet circumstances at 220 °C, (i) Contrast of NH<sub>3</sub> conversion in dry and wet circumstances at 240 °C.

ideal upshift would improve chemical and catalytic properties, which are usually more conducive to O<sub>2</sub> activation by depleting the outer orbitals electrons and increasing the density of states (DOS) of the anti-bonding  $\pi^*$  orbital. The H<sub>2</sub>-TPR experiment was used to study the redox properties of the samples, as shown in Fig. 6a. The reduction peak of adjacent TiO<sub>2</sub> oxides under the action of EMSI occurred at 186–207 °C [24]. Since the increase of the total CN of Ir cation will lead to the expansion of the difference in each bond length and bond energy, the reduction peak band shows a gradual broadening. The peak at 144 °C belongs to the reduction of adsorption activated O<sub>2</sub> at the interface of single-atom Ir<sub>1</sub> and the support, which changed with the number of interface sites. The reduction peak of oxygen species on the TiO<sub>2</sub> support cannot be observed within the temperature range of 50 °C–250 °C. This is because as a stable crystalline structure, it is difficult to form oxygen defects on the surface of rutile. In Fig. 6b, EPR spectra of all the Ir/TiO<sub>2</sub> samples with TEMP and DMPO spin trapping agent displayed 1: 1: 1 triplet and 1: 1: 1 quartet split signal, denoting the adsorption activated O<sub>2</sub> exists as singlet <sup>1</sup>O<sub>2</sub><sup>\*</sup> and superoxide O<sub>2</sub><sup>-</sup> species, respectively

[77,78].

The NH<sub>3</sub>-SCO performance of Ir/TiO<sub>2</sub> catalysts were evaluated in dry and wet circumstances. In Fig. 6c, NH<sub>3</sub> conversion (dry circumstance) over the 0.2Ir/TiO<sub>2</sub> catalyst started at 200 °C and reached 36% at 220 °C. As the Ir loading increases to 0.4 wt.% and 0.8 wt.%, the NH<sub>3</sub> conversion was 79% and even 100% at 220 °C, respectively. It can be seen that although a single-atom Ir<sub>1</sub> is an active site, TOF is not constant. The TOF of 0.8Ir/TiO<sub>2</sub>, 0.4Ir/TiO<sub>2</sub> and 0.2Ir/TiO<sub>2</sub> catalysts was  $1.01 \times 10^{-2} \text{ s}^{-1}$ ,  $0.57 \times 10^{-2} \text{ s}^{-1}$  and  $0.36 \times 10^{-2} \text{ s}^{-1}$ , respectively. The dehydrogenation of adsorbed NH<sub>3</sub> under the reaction of active oxygen species is the rate-determining step in the NH<sub>3</sub>-SCO reaction, which is influenced by both the NH<sub>3</sub> adsorption strength and oxygen activation ability. Among them, the active site is responsible for providing reactive oxygen species, while NH<sub>3</sub> adsorption strength is dominated by acid sites. Therefore, TOF would be affected by both active and acid sites, and the faster dehydrogenation rate of L-NH<sub>3</sub> promotes the reaction rate of NH<sub>3</sub> at the same active site. Tests conducted for 24 h revealed that the Ir/TiO<sub>2</sub> samples has excellent stability, and NH<sub>3</sub> conversion remained at

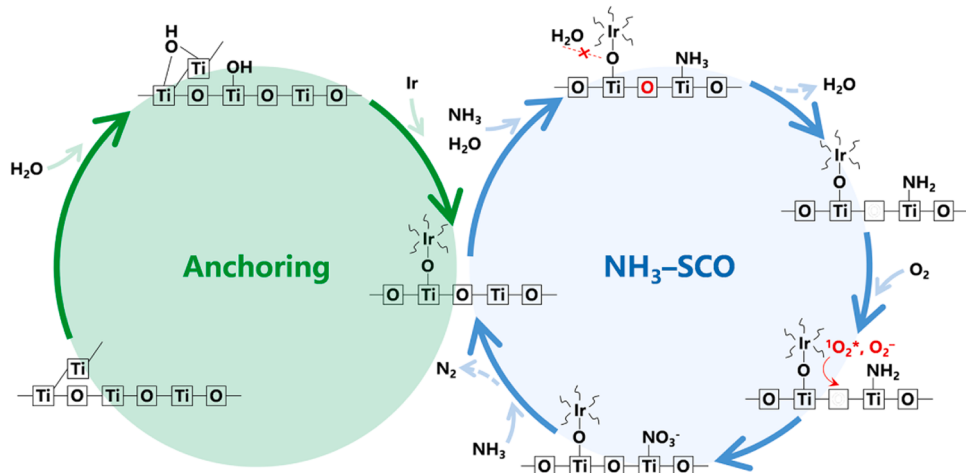


Fig. 7. Anchoring mechanism of active species on  $\text{TiO}_2$  and the  $\text{NH}_3\text{-SCO}$  reaction mechanism over  $\text{Ir}/\text{TiO}_2$  catalyst.

83%, 55%, and 19% at 210 °C on three samples. As well as there was almost no change in the aggregation and loading of active components under the reaction conditions, as shown in Fig. 6d. This indicates that the anchoring of Ir on the  $\text{TiO}_2$  surface is relatively stable. Meanwhile, the  $\text{N}_2$  selectivity was higher than 78% at 220 °C (Fig. 6e), and gradually decreased with increasing temperature. Within the experimental temperature range of 160 °C–360 °C,  $\text{NO}_x$  is the main by-product compared to  $\text{N}_2\text{O}$ . Especially in the temperature range of 220 °C to 360 °C, the conversion of  $\text{NH}_3$  to  $\text{NO}_x$  was significantly promoted, while the yield of  $\text{N}_2\text{O}$  remained below 20% (Fig. 6f–g). It is indicated that the peroxidation ability of catalysts is promoted at high temperatures, generating more unexpected by-products. We also found that a lower surface Ir loading on the catalyst is more favorable for the selective generation of  $\text{N}_2$ , which should be responsible by the corresponding relationship between  $\text{O}_2$  activation ability and Ir loading, as demonstrated by the  $\text{H}_2\text{-TPR}$  experiment. Although the rate-determining step is controlled by the difficulty of  $\text{O}_2$  activation, there should be an equilibrium between them. Once the nitrate species generate too fast and directly desorb without a secondary reaction with subsequent gas-phase  $\text{NH}_3$ , the generation of  $\text{NO}_x$  can be foreseen. Therefore, the appropriate  $\text{O}_2$  activation ability on the catalyst is crucial for improving  $\text{N}_2$  selectivity.

We further examined the  $\text{NH}_3\text{-SCO}$  performance of  $\text{Ir}/\text{TiO}_2$  catalysts in wet circumstance, and compared our results with previously reported catalytic systems (Fig. 6h–i and Table S4). On 0.2Ir/TiO<sub>2</sub> sample, 89%  $\text{NH}_3$  conversion dropped with the addition of 5%  $\text{H}_2\text{O}$  at 220 °C, while the descent rate was 87% or 72% for 0.4Ir/TiO<sub>2</sub> and 0.8Ir/TiO<sub>2</sub> samples. This indicates that water resistance is related to the amount of Ir loading. The superiority of 0.8Ir/TiO<sub>2</sub> sample in wet circumstance becomes more apparent at 240 °C, with the descent rate of  $\text{NH}_3$  conversion only decreasing by 15%, while the decrease rates of other samples are still above 60%. Our previous research has shown that the negative effect of water is due to the competitive adsorption of water molecules with  $\text{NH}_3$  [14]. According to other studies, water molecules are attracted and adsorbed on the surface of the material by forming hydrogen bondings with –OH groups [79]. We believe that the anchoring of Ir occupies and consumes the surface –OH groups of  $\text{TiO}_2$ , thereby reducing the competitive adsorption of water vapor, which is the main reason for the excellent water resistance in 0.8Ir/TiO<sub>2</sub>. This result is extremely similar to the water resistance of Ag based zeolites in wet conditions, as Al–OH is an important anchoring site for Ag cation [27,80]. It should be noted that the injection of water vapor also leads to a further increase in the yield of  $\text{NO}_x$ , resulting in lower  $\text{N}_2$  selectivity, particularly evident on the 0.8Ir/TiO<sub>2</sub> sample (presented in Fig. 6e and g). We speculate that although the lack of –OH groups reduce the competitive adsorption between  $\text{H}_2\text{O}$  and  $\text{NH}_3$  molecules, water vapor is likely to directly participate in the intermediate conversion process in gaseous form,

promoting the generation of nitrate species.

#### 4. Discussion

This work demonstrates that the –OH groups are the key sites for metal–support interactions that affect the morphology and dispersion of Ir species on  $\text{TiO}_2$ , and the activity and water resistance of the loaded  $\text{Ir}/\text{TiO}_2$  samples in the  $\text{NH}_3\text{-SCO}$  reaction. Based on measurements by HAADF-STEM, XAFS, EPR, XPS, in situ DRIFTS and DFT, we reveal that the Ir species anchor at the terminal –OH groups on  $\text{TiO}_2$  mainly through oxygen bridges. The source of the oxygen bridge is the coordinative saturation of the  $\text{Ti}_{5c}$  site through the interaction with  $\text{H}_2\text{O}$ . DFT calculations confirm that the binding energy of Ir in a multiple hydroxyl environment is as low as –11.83 eV, but still with the terminal –OH as anchoring center. The fitting results between the optimized model and XAFS confirmed that the CN of Ir–O bond was close to 5, and the Ir–Ti coordination was dominant in the second shell. This is important evidence for the atomic-level dispersion of Ir species on the  $\text{TiO}_2$ , which caused by the amount of terminal –OH groups on the surface of rutile  $\text{TiO}_2$  are as high as 75.4%. The consumption of –OH groups on  $\text{Ir}/\text{TiO}_2$  samples varies linearly with the increase of Ir loading, resulting in the more active coordinated L–NH<sub>3</sub> gradually becoming dominant.

The adsorption strength of  $\text{NH}_3$  is another key factor affecting the reaction rate-determining step, namely  $\text{NH}_3$  dehydrogenation, which has a significant contribution to improving the low-temperature activity of  $\text{NH}_3\text{-SCO}$ . On the one hand, the dehydrogenation rate of L–NH<sub>3</sub> is higher than that of B–NH<sub>4</sub><sup>+</sup>, which significantly increases the reaction rate of  $\text{NH}_3$  at a single active site by promoting the low-temperature formation of bidentate and bridging nitrates. The active oxygen species involved in this process include  $\text{O}_{\text{latt}}$  and singlet  $^1\text{O}_2^*$  or superoxide  $\text{O}_2^-$  species at the interface, under the reaction of EMSI between support and Ir cation. Afterwards, the reaction follows the i-SCR mechanism, and all nitrate intermediates are reduced by subsequent  $\text{NH}_3$ , achieving high  $\text{N}_2$  selectivity. The relevant reaction process is illustrated in Fig. 7. On the other hand, the coordinated L–NH<sub>3</sub> significantly avoids the competitive adsorption of water vapor in the  $\text{NH}_3\text{-SCO}$  reaction by reducing the number of hydrogen bonding. Since the strong ability of the catalysts to adsorb water is attributed to the formation of hydrogen bondings through –OH groups, and the amount of –OH groups on the  $\text{TiO}_2$  surface is balanced by loading highly dispersed Ir species.

#### 5. Conclusions

In summary, this work has studied that the –OH groups, as an important anchoring site for the dispersion and stability of Ir species on  $\text{TiO}_2$ , plays a decisive role in the reaction rate-determining step, namely

NH<sub>3</sub> dehydrogenation in NH<sub>3</sub>-SCO reactions. The 0.8Ir/TiO<sub>2</sub> sample shows higher reaction rate of NH<sub>3</sub> at a single active site and lower competitive adsorption of water vapor than 0.2Ir/TiO<sub>2</sub> and 0.4Ir/TiO<sub>2</sub>, attributed to the highest L-NH<sub>3</sub> ratio. Finally, the NH<sub>3</sub> conversion is 85% in a wet circumstance (5% H<sub>2</sub>O) at 240 °C (GHSV = 85 000 h<sup>-1</sup>), with a N<sub>2</sub> selectivity of up to 65% on 0.8Ir/TiO<sub>2</sub> sample. These results suggest that the adsorption strength of NH<sub>3</sub> is another influencing factor that besides O<sub>2</sub> activation and plays an important role in the NH<sub>3</sub>-SCO reaction rate-determining step. On the other hand, it further guides the synthesis of high-utilization metals on vacancy-deficient reducible oxides.

### CRediT authorship contribution statement

**Xu Wenqing:** Project administration, Resources, Writing – review & editing, Software. **Wang Yixi:** Validation, Visualization, Writing – original draft. **He Hong:** Writing – review & editing. **Yang Jun:** Writing – review & editing. **Yang Yang:** Writing – review & editing, Formal analysis. **Ma Jinzhu:** Software, Writing – review & editing. **Li Chaoqun:** Formal analysis, Methodology. **Zhu Tingyu:** Project administration, Resources, Supervision, Software.

### Declaration of Competing Interest

The authors declare that they have no known competing financial interests or personal relationships that could have appeared to influence the work reported in this paper.

### Data Availability

Data will be made available on request.

### Acknowledgements

This work was financially supported by the National Natural Science Foundation of China (No. 52070180, 52222005).

### Appendix A. Supporting information

Supplementary data associated with this article can be found in the online version at [doi:10.1016/j.apcatb.2023.123684](https://doi.org/10.1016/j.apcatb.2023.123684).

### References

- [1] L.P. Han, S.X. Cai, M. Gao, J. Hasegawa, P.L. Wang, J.P. Zhang, L.Y. Shi, D. S. Zhang, Selective catalytic reduction of NO<sub>x</sub> with NH<sub>3</sub> by using novel catalysts: State of the art and future prospects, *Chem. Rev.* 119 (2019) 10916–10976, <https://doi.org/10.1021/acs.chemrev.9b00202>.
- [2] K. Guo, J.W. Ji, W. Song, J.F. Sun, C.J. Tang, L. Dong, Conquering ammonium bisulfate poison over low-temperature NH<sub>3</sub>-SCR catalysts: a critical review, *Appl. Catal. B: Environ.* 297 (2021) 120388, <https://doi.org/10.1016/j.apcatb.2021.120388>.
- [3] T. Andana, R.K. G, F. Gao, J. Szanyi, X. Pereira-Hernandez, Y. Wang, Recent advances in hybrid metal oxide-zeolite catalysts for low-temperature selective catalytic reduction of NO<sub>x</sub> by ammonia, *Appl. Catal. B: Environ.* 291 (2021) 120054, <https://doi.org/10.1016/j.apcatb.2021.120054>.
- [4] C.M. Chen, Y. Cao, S.T. Liu, J.M. Chen, W.B. Jia, Review on the latest developments in modified vanadium-titanium-based SCR catalysts, *Chin. J. Catal.* 39 (2018) 1347–1365, [https://doi.org/10.1016/s1872-2067\(18\)63090-6](https://doi.org/10.1016/s1872-2067(18)63090-6).
- [5] M. Jabłońska, R. Palkovits, Copper based catalysts for the selective ammonia oxidation into nitrogen and water vapour-recent trends and open challenges, *Appl. Catal. B: Environ.* 181 (2016) 332–351, <https://doi.org/10.1016/j.apcatb.2015.07.017>.
- [6] Y.K. Yu, D.S. Wei, Z.J. Tong, J.X. Wang, J.S. Chen, C. He, Rationally engineered ReO-CuSO<sub>4</sub>/TiO<sub>2</sub> catalyst with superior NH<sub>3</sub>-SCO efficiency and remarkably boosted SO<sub>2</sub> tolerance: synergy of acid sites and surface adsorbed oxygen, *Chem. Eng. J.* 442 (2022) 136356, <https://doi.org/10.1016/j.cej.2022.136356>.
- [7] C.M. Chen, Y. Cao, S.T. Liu, J.M. Chen, W.B. Jia, SCR catalyst doped with copper for synergistic removal of slip ammonia and elemental mercury, *Fuel Process. Technol.* 181 (2018) 268–278, <https://doi.org/10.1016/j.fuproc.2018.09.025>.
- [8] Y. Liao, Z.S. Liu, Z.H. Li, G.Q. Gao, L.P. Ji, H.M. Xu, W.J. Huang, Z. Qu, N.Q. Yan, The unique CO activation effects for boosting NH<sub>3</sub> selective catalytic oxidation over CuO<sub>x</sub>-CeO<sub>2</sub>, *Environ. Sci. Technol.* 56 (2022) 10402–10411, <https://doi.org/10.1021/acs.est.2c02612>.
- [9] Z. Wang, Z.P. Qu, X. Quan, Z. Li, H. Wang, R. Fan, Selective catalytic oxidation of ammonia to nitrogen over CuO-CeO<sub>2</sub> mixed oxides prepared by surfactant-templated method, *Appl. Catal. B: Environ.* 134–135 (2013) 153–166, <https://doi.org/10.1016/j.apcatb.2013.01.029>.
- [10] J.Y. Liu, M.M. Sun, Q.J. Lin, S. Liu, H.D. Xu, Y.Q. Chen, Promotional effects of ethylenediamine on the low-temperature catalytic activity of selective catalytic oxidation of ammonia over Pt/SiAlO<sub>x</sub>: states and particle sizes of Pt, *Appl. Surf. Sci.* 481 (2019) 1344–1351, <https://doi.org/10.1016/j.apsusc.2019.03.199>.
- [11] E.M. Slavinskaya, L.S. Kibis, S.A. Stankus, D.A. Svintsitskiy, A.I. Stadnichenko, E. A. Fedorova, A.V. Romanenko, V. Marchuk, D.E. Doronkin, A.I. Boronin, The effects of platinum dispersion and Pt state on catalytic properties of Pt/Al<sub>2</sub>O<sub>3</sub> in NH<sub>3</sub> oxidation, *ChemCatChem* 13 (2020) 313–327, <https://doi.org/10.1002/cctc.202001320>.
- [12] H.F. Wang, T. Murayama, M.Y. Lin, N. Sakaguchi, M. Haruta, H. Miura, T. Shishido, Understanding the distinct effects of Ag nanoparticles and highly dispersed Ag species on N<sub>2</sub> selectivity in NH<sub>3</sub>-SCO reaction, *ACS Catal.* (2022) 6108–6118, <https://doi.org/10.1021/acs.catal.1c05762>.
- [13] F. Wang, G.Z. He, B. Zhang, M. Chen, X.Y. Chen, C.B. Zhang, H. He, Insights into the activation effect of H<sub>2</sub> pretreatment on Ag/Al<sub>2</sub>O<sub>3</sub> catalyst for the selective oxidation of ammonia, *ACS Catal.* 9 (2019) 1437–1445, <https://doi.org/10.1021/acs.catal.8b03744>.
- [14] Y.X. Wang, W.Q. Xu, X.Y. Chen, C.Q. Li, J. Xie, Y. Yang, T.Y. Zhu, C.B. Zhang, Single-atom Ir<sub>1</sub> supported on rutile TiO<sub>2</sub> for excellent selective catalytic oxidation of ammonia, *J. Hazard. Mater.* 432 (2022) 128670–128681, <https://doi.org/10.1016/j.jhazmat.2022.128670>.
- [15] L.L. Han, H. Cheng, W. Liu, H.Q. Li, P.F. Ou, R.Q. Lin, H.T. Wang, C.W. Pao, A. R. Head, C.H. Wang, X. Tong, C.J. Sun, W.F. Pong, J. Luo, J.C. Zheng, H.L. Xin, A single-atom library for guided monometallic and concentration-complex multimetallic designs, *Nat. Mater.* 21 (2022) 681–688, <https://doi.org/10.1038/s41563-022-01252-y>.
- [16] H.Y. Gu, X. Liu, X.F. Liu, C.C. Ling, K. Wei, G.M. Zhan, Y.B. Guo, L.Z. Zhang, Adjacent single-atom irons boosting molecular oxygen activation on MnO<sub>2</sub>, *Nat. Commun.* 12 (2021) 5422–5430, <https://doi.org/10.1038/s41467-021-25726-w>.
- [17] S.F. Ji, Y.J. Chen, X.L. Wang, Z.D. Zhang, D.S. Wang, Y.D. Li, Chemical synthesis of single atomic site catalysts, *Chem. Rev.* 120 (2020) 11900–11955, <https://doi.org/10.1021/acs.chemrev.9b00818>.
- [18] X. Zhou, I. Hwang, O. Tomanec, D. Fehn, A. Mazare, R. Zboril, K. Meyer, P. Schmuki, Advanced photocatalysts: pinning single atom co-catalysts on titania nanotubes, *Adv. Funct. Mater.* 31 (2021) 2102843–2102850, <https://doi.org/10.1002/adfm.202102843>.
- [19] J.Y. Chen, Y.J. Wanyan, J.X. Zeng, H.H. Fang, Z.J. Li, Y.D. Dong, R.X. Qin, C.Z. Wu, D.Y. Liu, M.Z. Wang, Q. Kuang, Z.X. Xie, L.S. Zheng, Surface engineering protocol to obtain an atomically dispersed Pt/CeO<sub>2</sub> catalyst with high activity and stability for CO oxidation, *ACS Sustain. Chem. Eng.* 6 (2018) 14054–14062, <https://doi.org/10.1021/acsschemeng.8b02613>.
- [20] W.T. Figueiredo, R. Prakash, C.G. Vieira, D.S. Lima, V.E. Carvalho, E.A. Soares, S. Buchner, H. Raschke, O.W. Perez-Lopez, D.L. Baptista, R. Hergenröder, M. Segala, F. Bernardi, New insights on the electronic factor of the SMSI effect in Pd/TiO<sub>2</sub> nanoparticles, *Appl. Surf. Sci.* 574 (2022) 151647–151654, <https://doi.org/10.1016/j.apsusc.2021.151647>.
- [21] N. Lopez, J.K. Nørskov, T.V.W. Janssens, A. Carlsson, A. Puig-Molina, B.S. Clausen, J.D. Grunwaldt, The adhesion and shape of nanosized Au particles in a Au/TiO<sub>2</sub> catalyst, *J. Catal.* 225 (2004) 86–94, <https://doi.org/10.1016/j.jcat.2004.03.036>.
- [22] Z.N. Wu, I. Hwang, G. Cha, S.S. Qin, O. Tomanec, Z. Badura, S. Kment, R. Zboril, P. Schmuki, Optimized Pt single atom harvesting on TiO<sub>2</sub> nanotubes-towards a most efficient photocatalyst, *Small* 18 (2022) e2104892–e2104899, <https://doi.org/10.1002/smll.202104892>.
- [23] J. Wang, W. Zhang, W.Y. Zhu, W.C. Zhuang, M. Lei, Rutile TiO<sub>2</sub> supported single atom Au catalyst: a facile approach to enhance methanol dehydrogenation, *Mol. Catal.* 482 (2020) 110670–110675, <https://doi.org/10.1016/j.mcat.2019.110675>.
- [24] S. Hoang, Y.B. Guo, A.J. Binder, W.X. Tang, S.B. Wang, J.Y. Liu, T.D. Huan, X.X. Lu, Y. Wang, Y. Ding, E.A. Kyriakidou, J. Yang, T.J. Toops, T.J. Pauly, R. Ramprasad, P.X. Gao, Activating low-temperature diesel oxidation by single-atom Pt on TiO<sub>2</sub> nanowire array, *Nat. Commun.* 11 (2020) 1062–1072, <https://doi.org/10.1038/s41467-020-14816-w>.
- [25] J.H. Kwak, J.Z. Hu, D.H. Mei, C.W. Yi, D.H. Kim, C.H.F. Peden, L.F. Allard, J. Szanyi, Coordinatively unsaturated Al<sup>3+</sup> centers as binding sites for active catalyst phases of platinum on gamma-Al<sub>2</sub>O<sub>3</sub>, *Science* 325 (2009) 1670–1673, <https://doi.org/10.1126/science.1176745>.
- [26] V.V. Dutov, G.V. Mamontov, V.I. Zaikovskii, L.F. Liotta, O.V. Vodyankina, Low-temperature CO oxidation over Ag/SiO<sub>2</sub> catalysts: effect of OH/Ag ratio, *Appl. Catal. B: Environ.* 221 (2018) 598–609, <https://doi.org/10.1016/j.apcatb.2017.09.051>.
- [27] F. Wang, J.Z. Ma, S.H. Xin, Q. Wang, J. Xu, C.B. Zhang, H. He, X.C. Zeng, Resolving the puzzle of single-atom silver dispersion on nanosized gamma-Al<sub>2</sub>O<sub>3</sub> surface for high catalytic performance, *Nat. Commun.* 11 (2020) 529–538, <https://doi.org/10.1038/s41467-019-13937-1>.
- [28] N.Q. Zhang, L.C. Li, Y.Z. Guo, J.D. He, R. Wu, L.Y. Song, G.Z. Zhang, J.S. Zhao, D. S. Wang, H. He, A MnO<sub>2</sub>-based catalyst with H<sub>2</sub>O resistance for NH<sub>3</sub>-SCR: Study of catalytic activity and reactants-H<sub>2</sub>O competitive adsorption, *Appl. Catal. B: Environ.* 270 (2020) 118860, <https://doi.org/10.1016/j.apcatb.2020.118860>.
- [29] K.A. Tarach, M. Jabłońska, K. Pyra, M. Liebau, B. Reiprich, R. Gläser, K. Góra-Marek, Effect of zeolite topology on NH<sub>3</sub>-SCR activity and stability of Cu-

exchanged zeolites, *Appl. Catal. B: Environ.* 284 (2021) 119752, <https://doi.org/10.1016/j.apcatb.2020.119752>.

[30] A.G. Thomas, W.R. Flavell, A.K. Mallick, A.R. Kumarasinghe, D. Tsoutsou, N. Khan, C. Chatwin, S. Rayner, G.C. Smith, R.L. Stockbauer, S. Warren, T.K. Johal, S. Patel, D. Holland, A. Taleb, F. Wiame, Comparison of the electronic structure of anatase and rutile  $\text{TiO}_2$  single-crystal surfaces using resonant photoemission and x-ray absorption spectroscopy, *Phys. Rev. B* 75 (2007) 035105–035116, <https://doi.org/10.1103/PhysRevB.75.035105>.

[31] C.X. Liu, L. Chen, J.H. Li, L. Ma, H. Arandiyani, Y. Du, J.Y. Xu, J.M. Hao, Enhancement of activity and sulfur resistance of  $\text{CeO}_2$  supported on  $\text{TiO}_2\text{-SiO}_2$  for the selective catalytic reduction of  $\text{NO}$  by  $\text{NH}_3$ , *Environ. Sci. Technol.* 46 (2012) 6182–6189, <https://doi.org/10.1021/es3001773>.

[32] P.D. Nellist, S.J. Pennycook, The principles and interpretation of annular dark-field Z-contrast imaging, *Adv. Imaging Electron Phys.* 113 (2000) 147–203, [https://doi.org/10.1016/S1076-5670\(00\)80013-0](https://doi.org/10.1016/S1076-5670(00)80013-0).

[33] L. Wang, B.F. Ji, Y.P. Zheng, Y.B. Tang, Asymmetric coordination of Iridium single-atom  $\text{IrN}_3\text{O}$  boosting formic acid oxidation catalysis, *Angew. Chem. Int. Ed.* (2023) e202301711, <https://doi.org/10.1002/anie.202301711>.

[34] B. Ravel, M. Newville, Athena, artemis, hephaestus: data analysis for X-ray absorption spectroscopy using ifeffit, *J. Synchrotron Radiat.* 12 (2005) 537–541, <https://doi.org/10.1107/S0909049505012179>.

[35] W.Y. Qu, H.Y. Yuan, Z.H. Ren, J.Z. Qi, D.R. Xu, J.X. Chen, L.W. Chen, H.G. Yang, Z. Ma, X. Liu, H.F. Wang, X.F. Tang, An Atom-pair design strategy for optimizing the synergistic electron effects of catalytic sites in  $\text{NO}$  selective reduction, *Angew. Chem. Int. Ed.* 61 (2022) e202212703, <https://doi.org/10.1002/anie.202212703>.

[36] H. Liu, J.N. Cheng, W.J. He, Y. Li, J. Mao, X.R. Zheng, C. Chen, C.X. Cui, Q.Y. Hao, Interfacial electronic modulation of  $\text{Ni}_3\text{S}_2$  nanosheet arrays decorated with Au nanoparticles boosts overall water splitting, *Appl. Catal. B: Environ.* 304 (2022) 120935, <https://doi.org/10.1016/j.apcatb.2021.120935>.

[37] Y.M. Zhu, J.A. Wang, T. Koketsu, M. Kroschel, J.M. Chen, S.Y. Hsu, G. Henkelman, Z.W. Hu, P. Strasser, J.W. Ma, Iridium single atoms incorporated in  $\text{Co}_3\text{O}_4$  efficiently catalyze the oxygen evolution in acidic conditions, *Nat. Commun.* 13 (2022) 7754, <https://doi.org/10.1038/s41467-022-35426-8>.

[38] A.Y. Ahmed, T.A. Kandiel, T. Oekermann, C. Günemann, D. Bahnemann, Mechanistic investigations of photoelectrochemical water and methanol oxidation on well-defined  $\text{TiO}_2$  anatase (101) and rutile (110) surfaces, *ACS Appl. Energy Mater.* 2 (2019) 5308–5318, <https://doi.org/10.1021/acsae.9b01163>.

[39] Y.J. Cao, S.J. Hu, M. Yu, S.S. Yan, M.C. Xu, Adsorption and interaction of  $\text{CO}_2$  on rutile  $\text{TiO}_2$ (110) surfaces: a combined UHV-FTIR and theoretical simulation study, *Phys. Chem. Chem. Phys.* 17 (2015) 23994–24000, <https://doi.org/10.1039/c5cp04013b>.

[40] Y. Adachi, Y. Sugawara, Y.J. Li, Probing CO on a rutile  $\text{TiO}_2$ (110) surface using atomic force microscopy and Kelvin probe force microscopy, *Nano Res.* 15 (2022) 1909–1915, <https://doi.org/10.1007/s12274-021-3809-x>.

[41] L. Li, W.S. Li, C.Y. Zhu, L.F. Mao, A DFT+U study about agglomeration of Au atoms on reduced surface of rutile  $\text{TiO}_2$  (110), *Mater. Chem. Phys.* 271 (2021) 124944–124951, <https://doi.org/10.1016/j.matchemphys.2021.124944>.

[42] M. Reticcioli, I. Sokolovic, M. Schmid, U. Diebold, M. Setvin, C. Franchini, Interplay between adsorbates and polarons: CO on rutile  $\text{TiO}_2$ (110), *Phys. Rev. Lett.* 122 (2019) 016805–016810, <https://doi.org/10.1103/PhysRevLett.122.016805>.

[43] M. Reticcioli, M. Setvin, M. Schmid, U. Diebold, C. Franchini, Formation and dynamics of small polarons on the rutile  $\text{TiO}_2$ (110) surface, *Phys. Rev. B* 98 (2018) 045306–045319, <https://doi.org/10.1103/PhysRevB.98.045306>.

[44] X.L. Hu, J.Y. Song, J.L. Luo, H. Zhang, Z.M. Sun, C.Q. Li, S.L. Zheng, Q.X. Liu, Single-atomic Pt sites anchored on defective  $\text{TiO}_2$  nanosheets as a superior photocatalyst for hydrogen evolution, *J. Energy Chem.* 62 (2021) 1–10, <https://doi.org/10.1016/j.jechem.2021.03.003>.

[45] J.L. Li, M. Zhang, Z.J. Guan, Q.Y. Li, C.Q. He, J.J. Yang, Synergistic effect of surface and bulk single-electron-trapped oxygen vacancy of  $\text{TiO}_2$  in the photocatalytic reduction of  $\text{CO}_2$ , *Appl. Catal. B: Environ.* 206 (2017) 300–307, <https://doi.org/10.1016/j.apcatb.2017.01.025>.

[46] Z.S. Han, C. Choi, S. Hong, T.S. Wu, Y.L. Soo, Y.S. Jung, J.S. Qiu, Z.Y. Sun, Activated  $\text{TiO}_2$  with tuned vacancy for efficient electrochemical nitrogen reduction, *Appl. Catal. B: Environ.* 257 (2019) 117896–117904, <https://doi.org/10.1016/j.apcatb.2019.117896>.

[47] G. Ou, Y.S. Xu, B. Wen, R. Lin, B.H. Ge, Y. Tang, Y.W. Liang, C. Yang, K. Huang, D. Zu, R. Yu, W.X. Chen, J. Li, H. Wu, L.M. Liu, Y.D. Li, Tuning defects in oxides at room temperature by lithium reduction, *Nat. Commun.* 9 (2018) 1302–1310, <https://doi.org/10.1038/s41467-018-03765-0>.

[48] F. Jiang, S.S. Wang, B. Liu, J. Liu, L. Wang, Y. Xiao, Y.B. Xu, X.H. Liu, Insights into the influence of  $\text{CeO}_2$  crystal facet on  $\text{CO}_2$  hydrogenation to methanol over Pd/ $\text{CeO}_2$  catalysts, *ACS Catal.* 10 (2020) 11493–11509, <https://doi.org/10.1021/acscatal.0c03324>.

[49] X. Yu, C.W. Hu, P.X. Ji, Y.M. Ren, H.Y. Zhao, G. Liu, R. Xu, X.D. Zhu, Z.Q. Li, Y.Q. Ma, L. Ma, Optically transparent ultrathin NiCo alloy oxide film: Precise oxygen vacancy modulation and control for enhanced electrocatalysis of water oxidation, *Appl. Catal. B: Environ.* 310 (2022) 121301–121311, <https://doi.org/10.1016/j.apcatb.2022.121301>.

[50] B.J. Morgan, G.W. Watson, Intrinsic n-type defect formation in  $\text{TiO}_2$ : a comparison of rutile and anatase from GGA+U calculations, *J. Phys. Chem. C* 114 (2010) 2321–2328, <https://doi.org/10.1021/jp9088047>.

[51] J.X. Chen, X. Fang, Z.H. Ren, W.Y. Qu, X.L. Hu, Z. Ma, L.W. Chen, X. Liu, Y.X. Chen, X.F. Tang, Single Mo atoms paired with neighbouring Ti atoms catalytically decompose ammonium bisulfate formed in low-temperature SCR, *J. Mater. Chem. A* 10 (2022) 6065–6072, <https://doi.org/10.1039/d1ta08269n>.

[52] X.C. Sun, J. Lin, Y.H. Wang, L. Li, X.L. Pan, Y. Su, X.D. Wang, Catalytically active  $\text{Ir}^0$  species supported on  $\text{Al}_2\text{O}_3$  for complete oxidation of formaldehyde at ambient temperature, *Appl. Catal. B: Environ.* 268 (2020) 118741–118751, <https://doi.org/10.1016/j.apcatb.2020.118741>.

[53] A.A. Tsyganenko, V.N. Filimonov, Infrared spectra of surface hydroxyl groups and crystalline structure of oxides, *Spectrosc. Lett.* 5 (1972) 477–487, <https://doi.org/10.1080/00387017208065418>.

[54] K.E. Lewis, G.D. Parfitt, Infra-red study of the surface of rutile, *Trans. Faraday Soc.* 62 (1966) 204–214, <https://doi.org/10.1039/TF9666200204>.

[55] L.Y. Ding, M. Li, Y.K. Zhao, H.N. Zhang, J.T. Shang, J.B. Zhong, H. Sheng, C. C. Chen, J.C. Zhao, The vital role of surface Brønsted acid/base sites for the photocatalytic formation of free-OH radicals, *Appl. Catal. B: Environ.* 266 (2020) 118634–118641, <https://doi.org/10.1016/j.apcatb.2020.118634>.

[56] T. Noda, K. Suzuki, N. Katada, M. Niwa, Combined study of IRMS-TPD measurement and DFT calculation on Brønsted acidity and catalytic cracking activity of cation-exchanged  $\text{Y}$  zeolites, *J. Catal.* 259 (2008) 203–210, <https://doi.org/10.1016/j.jcat.2008.08.004>.

[57] P. Jackson, G.D. Parfitt, Infra-red study of the surface properties of rutile. Water and surface hydroxyl species, *Trans. Faraday Soc.* 67 (1971) 2469–2483, <https://doi.org/10.1039/tf9716702469>.

[58] Y.L. Shan, G.Z. He, J.P. Du, Y. Sun, Z.Q. Liu, Y. Fu, F.D. Liu, X.Y. Shi, Y.B. Yu, H. He, Strikingly distinctive  $\text{NH}_3$ -SCR behavior over  $\text{Cu-SSZ-13}$  in the presence of  $\text{NO}_2$ , *Nat. Commun.* 13 (2022) 4606–4615, <https://doi.org/10.1038/s41467-022-32136-z>.

[59] J.Y. Luo, F. Gao, K. Kamasamudram, N. Currier, C.H.F. Peden, A. Yezerski, New insights into  $\text{Cu/SSZ-13}$  SCR catalyst acidity. Part I: Nature of acidic sites probed by  $\text{NH}_3$  titration, *J. Catal.* 348 (2017) 291–299, <https://doi.org/10.1016/j.jcat.2017.02.025>.

[60] P. Sudarsanan, N.K. Gupta, B. Mallesham, N. Singh, P.N. Kalbande, B.M. Reddy, F. S. Bert, Supported  $\text{MoO}_x$  and  $\text{WO}_x$  solid acids for biomass valorization: Interplay of coordination chemistry, acidity, and catalysis, *ACS Catal.* 11 (2021) 13603–13648, <https://doi.org/10.1021/acscatal.1c03326>.

[61] M.S. Xie, F.F. Dai, H.X. Guo, P.Y. Du, X.R. Xu, J. Liu, Z. Zhang, X.Q. Lu, Improving electrocatalytic nitrogen reduction selectivity and yield by suppressing hydrogen evolution reaction via electronic metal-support interaction, *Adv. Energy Mater.* (2023) 2203032, <https://doi.org/10.1002/aenm.202203032>.

[62] Z.M. Liu, S.X. Zhang, J.H. Li, J.Z. Zhu, L.L. Ma, Novel  $\text{V}_2\text{O}_5\text{-CeO}_2\text{/TiO}_2$  catalyst with low vanadium loading for the selective catalytic reduction of  $\text{NO}_x$  by  $\text{NH}_3$ , *Appl. Catal. B: Environ.* 158–159 (2014) 11–19, <https://doi.org/10.1016/j.apcatb.2014.03.049>.

[63] Y. Zhang, M. Zhang, Y.C. Zang, H.J. Wang, C.X. Liu, L.H. Wei, Y.H. Wang, L.J. He, W.C. Wang, Z.Y. Zhang, R. Han, N. Ji, C.F. Song, X.B. Lu, D.G. Ma, Y.R. Sun, Q. L. Liu, Elimination of  $\text{NH}_3$  by interfacial charge transfer over the  $\text{Ag/CeSnO}_x$  tandem catalyst, *ACS Catal.* 13 (2023) 1449–1461, <https://doi.org/10.1021/acscatal.2c05226>.

[64] J. Zhang, Z.W. Huang, Y.Y. Du, X.M. Wu, H.Z. Shen, G.H. Jing, Alkali-poisoning-resistant  $\text{Fe}_2\text{O}_3\text{/MoO}_3\text{/TiO}_2$  catalyst for the selective reduction of  $\text{NO}$  by  $\text{NH}_3$ : the role of the  $\text{MoO}_3$  safety buffer in protecting surface active sites, *Environ. Sci. Technol.* 54 (2020) 595–603, <https://doi.org/10.1021/acs.est.9b06318>.

[65] L.J. Yan, F.L. Wang, P.L. Wang, S. Impeng, X.Y. Liu, L.P. Han, T.T. Yan, D.S. Zhang, Unraveling the unexpected offset effects of Cd and  $\text{SO}_2$  deactivation over  $\text{CeO}_2\text{-WO}_3\text{/TiO}_2$  catalysts for  $\text{NO}_x$  reduction, *Environ. Sci. Technol.* 54 (2020) 7697–7705, <https://doi.org/10.1021/acs.est.0c01749>.

[66] Q.L. Zhang, T.X. Zhang, F.T. Xia, Y.Q. Zhang, H.M. Wang, P. Ning, Promoting effects of acid enhancing on  $\text{N}_2$  selectivity for selectivity catalytic oxidation of  $\text{NH}_3$  over  $\text{RuO}_x\text{/TiO}_2$ : the mechanism study, *Appl. Surf. Sci.* 500 (2020) 144044–144055, <https://doi.org/10.1016/j.apsusc.2019.144044>.

[67] H.C. Sun, H. Wang, Z.P. Qu, Construction of  $\text{CuO/CeO}_2$  catalysts via the ceria shape effect for selective catalytic oxidation of ammonia, *ACS Catal.* 13 (2023) 1077–1088, <https://doi.org/10.1021/acscatal.2c05168>.

[68] M. Jabłońska, A.M. Beale, M. Nocuń, R. Palkovits, Ag-Cu based catalysts for the selective ammonia oxidation into nitrogen and water vapour, *Appl. Catal. B: Environ.* 232 (2018) 275–287, <https://doi.org/10.1016/j.apcatb.2018.03.029>.

[69] F.D. Liu, H. He, Y. Ding, C.B. Zhang, Effect of manganese substitution on the structure and activity of iron titanate catalyst for the selective catalytic reduction of  $\text{NO}$  with  $\text{NH}_3$ , *Appl. Catal. B: Environ.* 93 (2009) 194–204, <https://doi.org/10.1016/j.apcatb.2009.09.029>.

[70] X. Li, J.H. Li, Y. Peng, X.S. Li, K.Z. Li, J.M. Hao, Comparison of the structures and mechanism of arsenic deactivation of  $\text{CeO}_2\text{-MoO}_3$  and  $\text{CeO}_2\text{-WO}_3$  SCR catalysts, *J. Phys. Chem. C* 120 (2016) 18005–18014, <https://doi.org/10.1021/acs.jpcc.6b03687>.

[71] Z. Li, Y.J. Chen, S.F. Ji, Y. Tang, W.X. Chen, A. Li, J. Zhao, Y. Xiong, Y. Wu, Y. Gong, T. Yao, W. Liu, L.R. Zheng, J.C. Dong, Y. Wang, Z.B. Zhuang, W. Xing, C. T. He, C. Peng, W.C. Cheong, Q.H. Li, M.L. Zhang, Z. Chen, N.H. Fu, X. Gao, W. Zhu, J.W. Wan, J. Zhang, L. Gu, S.Q. Wei, P.J. Hu, J. Luo, J. Li, C. Chen, Q. Peng, X.F. Duan, Y. Huang, X.M. Chen, D.S. Wang, Y.D. Li, Iridium single-atom catalyst on nitrogen-doped carbon for formic acid oxidation synthesized using a general host-guest strategy, *Nat. Commun.* 12 (2020) 764–772, <https://doi.org/10.1038/s41557-020-0473-9>.

[72] W. Tan, S.H. Xie, D. Le, W.J. Diao, M.Y. Wang, K.B. Low, D. Austin, S. Hong, F. Gao, L. Dong, L. Ma, S.N. Ehrlich, T.S. Rahman, F.D. Liu, Fine-tuned local coordination environment of Pt single atoms on ceria controls catalytic reactivity, *Nat. Commun.* 13 (2022) 7070, <https://doi.org/10.1038/s41467-022-34797-2>.

[73] D.P. Xue, J.Q. Cheng, P.F. Yuan, B.A. Lu, H.C. Xia, C.C. Yang, C.L. Dong, H. Z. Zhang, F.Y. Shi, S.C. Mu, J.S. Hu, S.G. Sun, J.N. Zhang, Boron-tethering and

regulative electronic states around Iridium species for hydrogen evolution, *Adv. Funct. Mater.* 32 (2022), <https://doi.org/10.1002/adfm.202113191>.

[74] C.T. Campbell, Electronic perturbations, *N. Views* 4 (2012) 597–598, <https://doi.org/10.1038/nchem.1412>.

[75] J.R. Yang, W.H. Li, D.S. Wang, Y.D. Li, Electronic metal-support interaction of single-atom catalysts and applications in electrocatalysis, *Adv. Mater.* 32 (2020) 2003300–2003329, <https://doi.org/10.1002/adma.202003300>.

[76] P.P. Hu, Z.W. Huang, Z. Amghouz, M. Makkee, F. Xu, F. Kapteijn, A. Dikhtiarenko, Y.X. Chen, X. Gu, X.F. Tang, Electronic metal-support interactions in single-atom catalysts, *Angew. Commun.* 53 (2014) 3418–3421, <https://doi.org/10.1002/anie.201309248>.

[77] Y.R. Fang, Q. Zhang, H. Zhang, X.M. Li, W. Chen, J. Xu, H. Shen, J. Yang, C.Q. Pan, Y.H. Zhu, J.L. Wang, Z. Luo, L.M. Wang, X.D. Bai, F. Song, L.Z. Zhang, Y.B. Guo, Dual activation of molecular oxygen and surface lattice oxygen in single atom Cu<sub>1</sub>/TiO<sub>2</sub> catalyst for CO oxidation, *Angew. Chem. Int. Ed.* 61 (2022) e202212273, <https://doi.org/10.1002/anie.202212273>.

[78] B. Liu, B. Zhang, J. Ji, K. Li, J. Cao, Q. Feng, H. Huang, Effective regulation of surface bridging hydroxyls on TiO<sub>2</sub> for superior photocatalytic activity via ozone treatment, *Appl. Catal. B: Environ.* 304 (2022), <https://doi.org/10.1016/j.apcatb.2021.120952>.

[79] E.P. Ng, S. Mintova, Nanoporous materials with enhanced hydrophilicity and high water sorption capacity, *Microporous Mesoporous Mater.* 114 (2008) 1–26, <https://doi.org/10.1016/j.micromeso.2007.12.022>.

[80] S. Satokawa, Y.J. Kobayashi, H. Fujiki, Adsorptive removal of dimethylsulfide and t-butylmercaptan from pipeline natural gas fuel on Ag zeolites under ambient conditions, *Appl. Catal. B: Environ.* 56 (2005) 51–56, <https://doi.org/10.1016/j.apcatb.2004.06.022>.